KSCE Journal of Civil Engineering (2019) 23(12):5121-5132
Copyright ⓒ2019 Korean Society of Civil Engineers
DOI 10.1007/s12205-019-1281-x

Nuclear Power Engineering
pISSN 1226-7988, eISSN 1976-3808
www.springer.com/12205

Numerical Analyses of Local Damage of Concrete Slabs by Normal Impact of Deformable Solid Projectiles

Ling-Yu Xu*, Fei Cai, Ying-Ying Xue***, Chiaki Takahashi****, and Yong-Yi Li*******

Received June 27, 2018/Accepted September 29, 2019/Published Online November 5, 2019

Abstract

Deformable solid projectiles undergo projectile mushrooming during impact and thus are different from rigid and soft hollow projectiles; however, limited work has been conducted on the impact of deformable solid projectiles on concrete targets. In this study, an explicit dynamic finite element procedure is employed to study nine existing experimental tests on the normal impact of a deformable solid (lead) projectile into a plain concrete (PC) slab. To correctly model the impact, both non-linear material response and progressive finite element erosion have been taken into account for the deformable solid projectile and the PC slab. The numerical results are compared with experimental results in terms of different modes of local damage to the PC slab and the maximum penetration depth of the PC slab. The mechanism of the front cratering, the scabbing, and the perforation of concrete target under the impact of deformable solid projectile and the effect of projectile rigidity on the local damage to the PC slab are investigated. A dose-response relation is used to describe the variation of the maximum penetration depth with the impact velocity. Some model parameters that most affect the simulation results are also highlighted.

Keywords: *deformable solid projectile, projectile mushrooming, LS-DYNA, RHT concrete model, dose-response relation*

1. Introduction

Concrete is widely used for constructing both civil and military structures, such as nuclear power plant, bunkers, shelters and command centers, to resist the missile or projectile impact (Kennedy, 1976). The impacting missiles or projectiles are generally classified as either 'rigid (hard)' or 'soft' depending on whether the projectile deformability is small or large relative to the target deformability (Eibl, 1987) or depending on the material strength (target and projectile) and the projectile velocity (Koechlin and Potapov, 2009). Some experimental work has been carried out to investigate the effect of rigid projectile impacts and soft projectile impacts (Wen and Xian, 2015; Kojima *et al*., 1991; Ohno *et al*., 1992; Cox *et al*., 2006; Wilt *et al*., 2011; Pontiroli *et al*., 2012). In these tests, the front of soft projectiles is often designed to have a hemispherical nose or a thin rigid plate followed by a hollow tube to model an aircraft or the engine of an aircraft (Kojima *et al*., 1991; Ohno *et al*., 1992; Cox *et al*., 2006; Wilt *et al*., 2011; Pontiroli *et al*., 2012). Thus, the energy absorption resulting from the deformation of the hollow tube makes the amount of damage less than that caused by rigid projectiles. In reality, there are also deformable solid projectiles which undergo projectile mushrooming during impact and thus are different from rigid and soft hollow projectiles (Khoda-Rahmi *et al*., 2006). During impact, the nose of the soft hollow projectile almost remains unchanged, like the rigid projectile, or changes slightly due to the buckling of the hollow tube (Kojima *et al*., 1991; Ohno *et al*., 1992; Cox *et al*., 2006; Wilt *et al*., 2011; Pontiroli *et al*., 2012), while the nose of a deformable solid projectile expands, and the diameter of the deformed nose becomes much larger. Thus, it is expected that the damage to the concrete target caused by deformable solid projectiles is different from that caused by rigid and soft hollow projectiles. However, limited work has been conducted on the impact of deformable solid projectiles into concrete targets, especially the hypervelocity impact with an impact velocity on the order of 10^3 m/s (Hazell *et al*., 1998; Forrestal and Piekutowski, 2000; Chen and Li, 2004; Lou *et al*., 2014).

Finite element analysis has been proved to be an appropriate and efficient solution for the impact problems (Hong *et al*., 2018; Wang *et al*., 2007; Tai *et al*., 2011; Lv *et al*., 2018; Cui *et al*., 2018). In this study, an explicit dynamic finite element procedure LS-DYNA (LSTC, 2014) is employed to study nine experimental tests reported by Tanaka and Ohno (2004) on the normal impact of deformable solid (lead) projectiles into a PC slab. The Steinberg

---

*Lecturer, College of Transportation Science & Engineering, Nanjing Tech University, Nanjing 210009, China (Corresponding Author, E-mail: xulingyu2008@126.com)
**Associate Professor, Dept. of Environmental Engineering Science, Gunma University, Kiryu 376-8515, Japan (E-mail: feicai@gunma-u.ac.jp)
***Engineer, Earthquake Administration of Jiangsu Province, Nanjing 210014, China (E-mail: xyy285108@163.com)
****Project Manager, Pacific Consultants Co. Ltd., Tokyo 101-8462, Japan (E-mail: chiaki.takahashi@tk.pacific.co.jp)
*****Associate Professor, College of Transportation Science & Engineering, Nanjing Tech University, Nanjing 210009, China (E-mail: liyongyi@njtech.edu.cn)

model (#11) and the RHT concrete model (#272) available in LS-DYNA are used to characterize the dynamic response of the deformable solid projectile and the PC slab, respectively. The simulation results are compared with experimental results in terms of different modes of local damage to the PC slab and the maximum penetration depth of the PC slab. Based on the numerical results, the mechanism of the perforation of the PC slab under the impact of the deformable solid projectile is investigated. In addition, the effect of impact velocity of the deformable solid projectile on the maximum penetration depth of the PC slab and the effect of projectile rigidity on the local damage of the PC slab are studied. Some comments are made on the effect of the erosion parameters used for the deformable solid projectile and the damage parameters and uniaxial compressive strength used for the PC slab on the local damage of the PC slab.

2. Description of Impact Tests Conducted by Tanaka and Ohno

Tanaka and Ohno (2004) conducted a series of impact tests on both the normal and oblique impacts of deformable solid projectiles into a plain concrete slab. The facility of the impact test is shown in Fig. 1. The concrete slab was fixed in the range of 50 mm apart from both the top and bottom edges along the length direction. The size of the PC slab was 500 mm × 350 mm × t; t represents the thickness of the PC slab, i.e., 30 mm, 50 mm, 70 mm, and 100 mm, in all cases. The concrete mix proportioning used in the impact tests is presented in Table 1. The uniaxial compressive strength of the concrete reported by Tanaka and Ohno (2004) is 28.5 MPa, which is in a typical range of 15 MPa – 100 MPa that used by an empirical formula proposed by Li and Tong (2003), for estimating the perforation thickness of concrete target subjected to rigid projectile impact.

The solid projectile used in the test is made of lead. There were two types of deformable solid projectile used in the impact tests, i.e., Type A and Type B projectiles. In this study, the type-A projectile is selected for the simulation. The type-A projectile consists of a conical nose followed by a cylindrical body with a diameter of approximately 8 mm, as shown in Fig. 1. The mass of the type-A projectile was approximately 0.01 kg (Tanaka and Ohno, 2004).

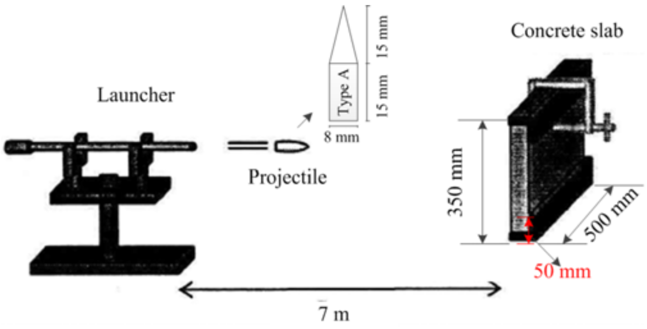

Fig. 1. Impact Test Facility (Tanaka and Ohno, 2004)

3. Proposed Finite Element Model

In this section, the proposed finite element model created in LS-DYNA is presented. In general, three numerical techniques are available in LS-DYNA for the analysis of impact problems, i.e., a mesh free method known as smooth particle hydrodynamics (SPH), a multi-material arbitrary Lagrange Eulerian technique (MM-ALE), and a Lagrangian technique with material erosion. In this study, the Lagrangian technique with material erosion technique is selected.

3.1 Element Type and Finite Element Mesh

A 2D axisymmetric solver is used for the numerical analyses by considering the PC slab to be a cylinder with a 35 cm diameter. A large number of elements will be required for the three-dimensional solver because the size of the deformable solid projectile is significantly smaller than that of the PC slab. Thus, the 2D axisymmetric solver allows for more comprehensive solutions. Note that the PC slab shown in Fig. 1 is rectangular in shape. The calculations indicate that the local damage of the PC slab is concentrated within 10 cm apart from the projectile for all cases analyzed. Thus, the diameter of 35 cm used in the 2D axisymmetric model for the PC slab is reasonably acceptable.

In the finite element analyses, an area-weighted axisymmetric solid element (*x*-*y* plane, *y*-axis of symmetry) is used. The details of the formulation of the area-weighted axisymmetric solid

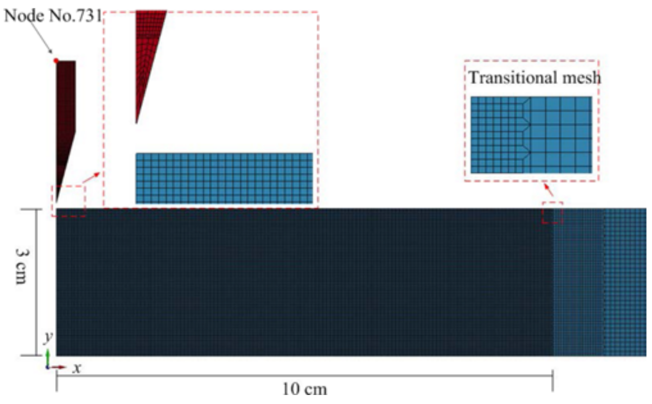

Fig. 2. Typical Finite Element Mesh for the Deformable Solid Projectile and the Plain Concrete Slab

Table 1. Mix Proportion of the Concrete Used in the Impact Tests Reported by Tanaka and Ohno (2004)

Maximum aggregate size (mm)	Slump (cm)	Water-cement ratio	Fine aggregate percentage	Ingredients of concrete (kg/m^3)				
				Water	Portland cement	Fine aggregate	Coarse aggregate	Admixtures
20	15	0.49	44.7	167	341	793	1,011	3.41

element can be found in Aquelet and Souli (2008). Fig. 2 shows the typical finite element mesh for the deformable solid projectile and the PC slab. The mesh size for the deformable solid projectile and the PC slab near the impact location ($0 \le x \le 10$ cm) is set to approximately 0.25 mm. Coarse meshes are used for the concrete outside the impact location via a transitional pyramid meshing technique to reduce the computation time, as shown in Fig. 2.

3.2 Material Model

3.2.1 Deformable Solid (Lead) Projectile

Lead is a soft and low strength metal; the solid state could be transformed to the liquid state during the impact because the temperature increases in the system can easily exceed the melting temperature of lead. Thus, a pressure-dependent model is more appropriate for the lead than a strain rate dependent one because the lead could be in a liquid state (Adams, 2003; Mohotti, 2013). In this study, a pressure-dependent model, i.e., the Steinberg model (#11), is used as the material model for the deformable solid projectile. This model was originally developed by Steinberg *et al*. (1980). The material parameters used for the lead in this study are from Steinberg *et al*. (1980) and are shown in Table 2. The shear modulus and the yield strength of the Steinberg model are determined by the following equations:

$$G = G_0\left[1+\left(\frac{G'_p}{G_0}\right)\frac{P}{\eta^{1/3}}-\left(\frac{G'_T}{G_0}\right)(T-300)\right]e^{\frac{-fE_i}{E_m-E_i}} \tag{1}$$

$$\sigma = \sigma_0\left[1+\beta(\varepsilon+\varepsilon_i)\right]^n\left[1+\left(\frac{G'_p}{G_0}\right)\frac{P}{\eta^{1/3}}-\left(\frac{G'_T}{G_0}\right)(T-300)\right]e^{\frac{-fE_i}{E_m-E_i}} \tag{2}$$

where,

$$\begin{cases} T = \dfrac{E_i - E_c}{3R'} \\ R' = \dfrac{R\rho_0}{A} \\ E_c(x) = \int_0^x P dx - \dfrac{900R'\exp(ax)}{(1-x)^{2(\gamma_0 - a - 1/2)}} \\ x = 1 - {}^1\!/_\eta \\ E_m(x) = E_c(x) + 3R'T_m(x) \\ T_m(x) = T_{m0}\exp(2ax)\eta^{2(\gamma_0 - a - 1/3)} \end{cases} \tag{3}$$

Here, η is the compression ratio that is defined as the initial specific volume υ_0 divided by the specific volume υ; β and n are work-hardening parameters, ε is the plastic strain, ε_0 is the initial plastic strain, normally equal to zero; G_0 and σ_0 are shear modulus and yield strength at the reference state ($T = 300$ K, $P = 0, \varepsilon = 0$); G_p, G_T, σ'_p, σ'_T are derivatives of G and σ with respect to pressure or temperature at the reference state, respectively; E_i, E_c, E_m are specific internal energy, specific cold compression energy, and specific melting energy, respectively; R is the gas constant; T_{m0} is the melting temperature; ρ_0 is the initial density; A is the atomic weight; γ_0 is the γ at the reference state, where γ is defined as $-\partial \ln T/\partial \ln \upsilon$ at constant entropy; a is the coefficient of first-order volume correction to γ, f is a model parameter and taken as 0.001 according to Lee and Painter (1999). Note that the value of the item $\sigma_0[1+\beta(\varepsilon+\varepsilon_i)]^n$ in Eq. (1) is limited to the maximum strength σ_m.

In addition to these material parameters, an equation of state is needed to describe the pressure-compaction curve representing the volumetric response behavior of the lead. In this study, the keyword *EOS_GRUNEISEN is used to define the equation of state; the parameters used for the lead are from Mohotti *et al*. (2013) and are listed in Table 3, where C is the intercept of the cubic shock velocity-particle velocity ($v_s - v_p$) curve; S_1, S_2, and S_3 are the coefficients of the slope of the $v_s - v_p$ curve, respectively; γ_0 is the Gruneisen gamma; and a is the first order volume correction to γ_0.

In addition to the Steinberg model (#11), element erosion is required to simulate the crushing of the deformable solid projectile. Element erosion is initiated by using the *MAT_ADD_EROSION option (LSTC, 2014). The maximum equivalent plastic strain at failure ε_{eff} is used for the erosion criterion and is defined as follows (LSTC, 2014):

$$\varepsilon_{eff} = \sqrt{2/3\,\varepsilon_{ij}^{dev}\varepsilon_{ij}^{dev}} \tag{4}$$

where ε_{ij}^{dev} is the deviatoric strain. The ε_{ff} erosion criterion is recommended for metallic materials, as suggested by Adams (2003) and Luccioni *et al*. (2013).

Elements that reach a user-specified value for the maximum equivalent plastic strain at failure are deleted from the calculation. The deformable solid projectile was strongly damaged during the impact; this results in a breaking away of smaller lead projectile fragments in the experiments reported by Tanaka and Ohno (2004). Thus, the erosion technique is used to reproduce the failure mechanism observed from the experiments, as also suggested by other research for the impact analysis (Pontiroli *et al*., 2012). A value of 2.0 is used for the maximum equivalent plastic strain at failure based on a parametric study that consists of running numerical simulations with different erosion strain values and observing the overall damage, as discussed in Section 5.5.

Table 3. Input Parameters for the Equation of State Defined by the Keyword *EOS_GRUNEISEN

Parameter	C (cm/μs)	S_1	S_2	S_3	γ_0	a
Value	0.2051	1.46	0	0	2.77	0

Table 2. Input Parameters for the Steinberg Model in the Cm-gram-microsecond System of Units for LS-DYNA

Parameters	G_0 (10^{11}Pa)	σ_0 (10^{11}Pa)	σ_m (10^{11}Pa)	β	n	G_p'/G_0 (10^{11}Pa)	G_T'/G_0 (K^{-1})	f	T_{m0}	A	γ_0	a
Value	0.086	0.00008	0.001	110	0.52	11.6	0.00116	0.001	760	82	2.74	2.2

3.2.2 PC Slab

The RHT concrete model (#272) is available in LS-DYNA via the keyword *MAT_RHT (LSTC, 2014) and is used to characterize the dynamic response of the PC slab. This model is widely used for the solution of concrete impact problems (Leppänen, 2006; Prakash *et al*., 2015). The model, consisting of the initial yield surface, failure surface, and residual friction surface, includes pressure hardening, strain hardening and strain rate hardening. In the RHT model, the pressure is described by the Mie-Gruneisen form with a polynomial Hugoniot curve and a p-α compaction relation.

The numerical results show that a higher uniaxial compressive strength of concrete should be used in the simulation to achieve the most comparable results of the maximum penetration depth of the PC slab. This may be a result of the fact that the diameter of the deformable solid projectile is much smaller than the maximum aggregate size in the concrete (i.e., 20 mm, see Table 1) and the strength of the coarse aggregate is normally larger than the macroscopic strength of the concrete as measured by the uniaxial compression test. Thus, the coarse aggregate may dominate the impact response of the PC slab because of its relatively large percentage in the concrete, as shown in Table 1. However, such a predominant effect of the coarse aggregate is complex and is currently not considered in most macroscopic constitutive models, including the RHT model used in this study. Another reason for the use of the higher uniaxial compressive strength may lie in the fact that the strength of the tested concrete slab may increase because of the effect of the curing time (Yi *et al*., 2005). A parametric study was performed by increasing the uniaxial compressive strength in the simulation and by observing the maximum penetration depth of the PC slab. The numerical results show that the use of 58 MPa for the uniaxial compressive strength of the concrete can give the most comparable results of the maximum penetration depth. The material parameters used in the analyses are listed in Table 4.

Table 4. Input Parameters for the RHT Concrete Model in the Cm-gram-microsecond System of units for LS-DYNA

Parameters	Value
Elastic shear modulus G (10^{11} Pa)	0.159[a]
Eroding plastic strain	2[b]
Parameter for polynomial EOS B_1	1.22[b]
Parameter for polynomial EOS B_2	1.22[b]
Parameter for polynomial EOS T_1	0.3527[b]
Parameter for polynomial EOS T_2	0.0[b]
Failure surface parameter A	1.6[b]
Failure surface parameter N	0.61[b]
Compressive strength f_c (10^{11} Pa)	0.00058
Relative shear strength f_s^*	0.18[b]
Relative tensile strength f_t^*	0.1[b]
Lode angle dependence factor Q_0	0.6805[b]
Lode angle dependence factor B	0.0105[b]
Reference compressive strain rate $\dot{\varepsilon}_0^c$ (μs^{-1})	3e-11[b]
Reference tensile strain rate $\dot{\varepsilon}_0^t$ (μs^{-1})	3e-12[b]
Break compressive strain rate	3e22[b]
Break tensile strain rate	3e22[b]
Compressive strain rate dependence exponent β_c	0.032[b]
Tensile strain rate dependence exponent β_t	0.036[b]
Volumetric plastic strain fraction in tension	0.001[b]
Compressive yield surface parameter g_c^*	0.53[b]
Tensile yield surface parameter g_t^*	0.70[b]
Shear modulus reduction factor	0.5[b]
Damage parameter D_1	0.24[c]
Damage parameter D_2	2.0[c]
Minimum damaged residual strain ε_p^m	0.01[b]
Residual surface parameter A_f	1.6[b]
Residual surface parameter n_f	0.61[b]
Gruneisen gamma γ_0	0.0[b]
Hugoniot polynomial coefficient A_1 (10^{11}Pa)	0.3527[b]
Hugoniot polynomial coefficient A_2 (10^{11}Pa)	0.3958[b]
Hugoniot polynomial coefficient A_3 (10^{11}Pa)	0.0904[b]
Crush pressure P_{el} (10^{11}Pa)	0.000233[b]
Compaction pressure P_{comp} (10^{11}Pa)	0.06[b]
Porosity exponent N	3.0[b]
Initial porosity α_0	1.1884[b]

[a]determined by Eq. (5); [b]default values reported by Borrvall and Riedel (2011); [c]adjusted according to Eq. (10) through parametric study.

Most of the parameters of the RHT concrete model use the default values reported by Borrvall and Riedel (2011) except for the shear modulus and other two damage parameters, i.e., D_1 and D_2. The shear modulus of concrete G is calculated by the following equation:

$$G = \frac{E}{2(1+\upsilon)} \tag{5}$$

where,

$$E = 5{,}000\sqrt{f_c}\ (in\ \text{MPa}) \tag{6}$$

where E is the elastic modulus of concrete and calculated by an empirical equation suggested by Chen and Duan (2003) and Xu *et al.* (2017), υ is Poisson's ratio and is set to 0.2 for concrete, and f_c is uniaxial compressive strength of concrete (in MPa).

The failure criterion is already included in the RHT model in terms of the plastic strain at failure ε_p^f and is given by the following equation:

$$\varepsilon_p^f = \begin{cases} D_1\left[p^* - (1-D)p_t^*\right]^{D_2} & p^* \geq (1-D)p_t^* + \left(\dfrac{\varepsilon_p^m}{D_1}\right)^{1/D_2} \\ \varepsilon_p^m & p^* < (1-D)p_t^* + \left(\dfrac{\varepsilon_p^m}{D_1}\right)^{1/D_2} \end{cases} \tag{7}$$

where D_1 and D_2 are two damage parameters, of which the determination is discussed in the next section; p^* is the pressure p divided by f_c; p_t^* is the failure cut-off pressure; ε_p^m is minimum damaged residual strain and is taken as the default value of 2.0; and D is the damage value and is accumulated with the incremental plastic strain $\Delta\varepsilon_p$ according to:

$$D = \sum \frac{\Delta\varepsilon_p}{\varepsilon_p^f} \tag{8}$$

The value of D lies between 0 and 1, indicating two extremes that do not damage the material and fully damage the material in tension, respectively. The damage value D is used to determine the value of the current strength surface after cementitious material begins to harden or soften, as expressed by the following equation.

$$\sigma_d\left(p^*\right) = \begin{cases} \sigma_y\left(p^*, \mathrm{s}, \dot{\varepsilon}_p, \varepsilon_p^*\right)(1-D) + Df_c A_f\left(p^*\right)^{n_f}, & p^* \geq 0 \\ \sigma_y\left(p^*, \mathrm{s}, \dot{\varepsilon}_p, \varepsilon_p^*\right)\left(1 - D - \dfrac{p^*}{p_t^*}\right), & (1-D)\,p_t^* \leq p^* < 0 \end{cases} \tag{9}$$

Where $\sigma_d(p^*)$ is the current strength surface, $\sigma_y(p^*, s, \dot{\varepsilon}_p, \varepsilon_p^*)$ is the elastic-plastic yield surface for the RHT model and is a function of p^*, the deviatoric stress tensor s, the incremental plastic strain $\dot{\varepsilon}_p$, a plastic strain ε_p^*. For a more detailed description see LSTC (2014). The damage value is often used to identity the cracking and scabbing of concrete subjected to impact loading (Prakash *et al*., 2015).

In this study, the damage parameters D_1 and D_2 are considered to be consistent and thus reasonably adjusted together by reforming Eq. (7) as follows; this is different from Prakash *et al*. (2015), in which only the damage parameter D_1 is increased.

$$D_1 = \frac{\varepsilon_p^f}{\left[p^* - (1-D)\,p_t^*\right]^{D_2}} \tag{10}$$

Here, $\varepsilon_p^f = 0.016$ and $p^* = 0.167$ are suggested by based on the experimental results of a 150 cm cubic piece of concrete with the compressive strength of approximately 40 MPa (Ding *et al*., 2013). The AUTODYN procedure uses the relative hydrostatic tensile strength f_{ttt}^* instead of the term $(1-D)p_t^*$ in Eq. (10) (Prakash *et al*., 2015; Ding *et al*., 2013). In this study $p_t^* = -0.09$ and $D = 0$ are used for the concrete in the initial state; thus, the term $(1-D)p_t^*$ has a value of -0.09, corresponding to $f_{ttt}^* = -0.09$ as suggested by Ding *et al*. (2013) to determine the damage parameters D_1 and D_2. To this end, D_1 is obtained by setting a value for D_2, as done for the determination of the parameters D_1 and D_2 in Table 4.

3.3 Contact and Boundary Conditions

The keyword *CONTACT_2D_AUTOMATIC_SINGLE_SURFACE option is used to create the contact between the deformable solid projectile and the PC slab (LSTC, 2014).

The nodes at the outer diameter of the axisymmetric model are fixed in the y-axis direction shown in Fig. 3. Such boundary conditions for the axisymmetric model are not the same as that in the impact test shown in Fig. 1, i.e., fixed-free. This is considered to be reasonable because the size of the deformable solid projectile is comparatively small, and thus the bending of the PC slab is considered to be negligible.

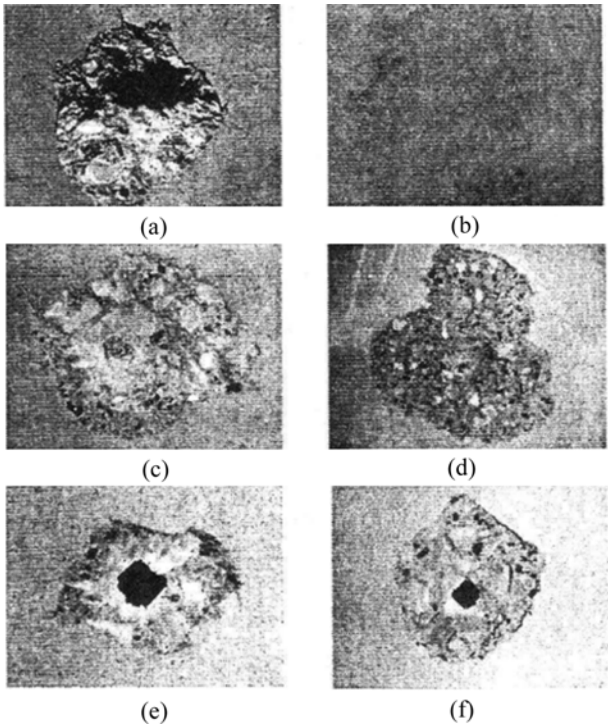

Fig. 3. Typical Damage of the Plain Concrete Slab: (a) Penetration (front face), (b) Penetration (rear face), (c) Scabbing (front face), (d) Scabbing (rear face), (e) Perforation (front face), (f) Perforation (rear face) (Tanaka and Ohno, 2004)

4. Verification of the Proposed Finite Element Model

Finite element analyses are performed on nine normal impact tests, as listed in Table 5. The typical local damage of the PC slab is categorized as perforation, scabbing, or penetration, as shown in Figs. 3(a), 3(b), and 3(c), respectively (Tanaka and Ohno, 2004). The proposed finite element model is verified by comparing the simulation results and experimental results in terms of different modes of local damage to the PC slab and the maximum penetration depth of the PC slab.

4.1 Simulated Maximum Penetration Depth in Combination with Typical Scabbing and Penetration Damage to the PC Slab

Table 2 presents the simulated and measured maximum penetration depth of the PC slab for five cases: Case 1-2, Case 1-3, Case 2-2, Case 2-3, and Case 3-3. The results show that the maximum penetration depth simulated by the proposed finite element model corresponds well with those measured in the test, demonstrating the capability of the proposed finite element model.

In addition to the maximum penetration depth, the local damage of the PC slab is also well simulated for these five cases. Figs. 4(a) and 4(b) shows the local damage of the PC slab in Case 2-3 and Case 2-2, representing the typical damage of

Table 5. Tests on Normal Impact of Type-A Deformable Solid Projectiles

Cases	Impact velocity (m/s)	*t* (cm)	Experimental damage mode	Maximum penetration depth (cm)	
				Experiment	Simulation
Case 1-1	337	3	Perforation	-	Perforation
Case 1-2	337	5	Penetration	0.64 – 0.9	0.86
Case 1-3	337	7	Penetration	0.64 – 0.9	0.82
Case 2-1	515	3	Perforation	-	Perforation
Case 2-2	515	5	Scabbing	1.8	1.83
Case 2-3	515	7	Penetration	1.3	1.73
Case 3-1	732	3	Perforation	-	Perforation
Case 3-2	732	5	Perforation	-	Perforation
Case 3-3	732	7	Scabbing	2.9	2.95

penetration and scabbing, respectively, in terms of the contour of the damage value *D*. Red indicates fully developed damage (i.e., $D = 1$). The results show that most of the deformable solid projectile erodes in these two cases, and some fragments of the deformable solid projectile rebound from the front crater of the PC slab. As for Case 2-3 shown in Fig. 4(a), some scabbing is developed at the rear face of the PC slab; however, the front crater formed at the front surface of the PC slab is much larger than the scabbing area. Considering the discrepancy between the simulation and the experiment, the damage of the PC slab in this case shows the overall characteristics of the experimental damage shown in Fig. 2(a); therefore, the damage of the PC slab in this case is clarified as penetration. As for Case 2-2 shown in Fig. 4(b), not only the front cratering is formed at the front surface of the PC slab, but additionally, notable scabbing is developed at the rear face of the PC slab. The simulated damage of the PC slab agrees well with the observed damage of the PC slab, i.e., scabbing, as shown in Figs. 3(c) and 3(d).

Moreover, the rebound of the projectile can also be identified from Fig. 5(a) which shows that the projectile velocities of a typical node (i.e., Node No. 731 shown in Fig. 2) in most cases in question decrease to a small negative value in the simulation. In addition, the nodal velocity of the projectile decreases more rapidly

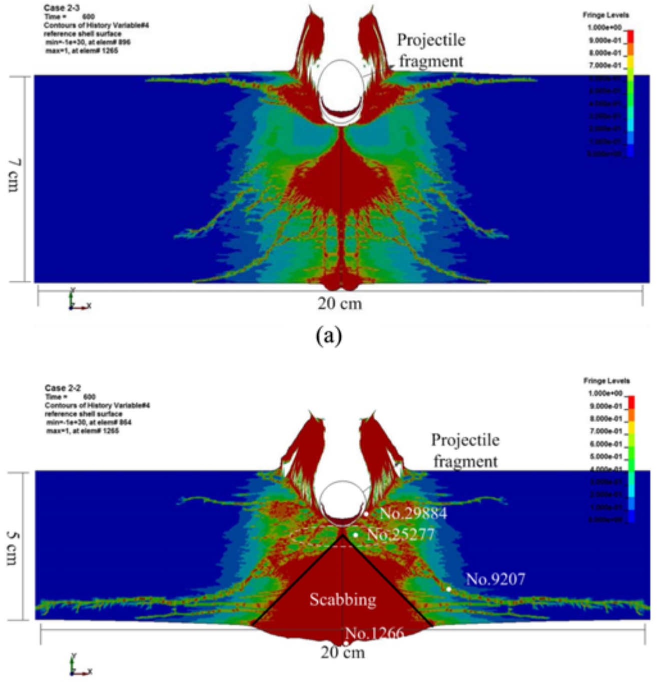

(a)

(b)

Fig. 4. Simulated Local Damage of the Plain Concrete Slab for: (a) Case 2-3, (b) Case 2-2 Shown in Table 1

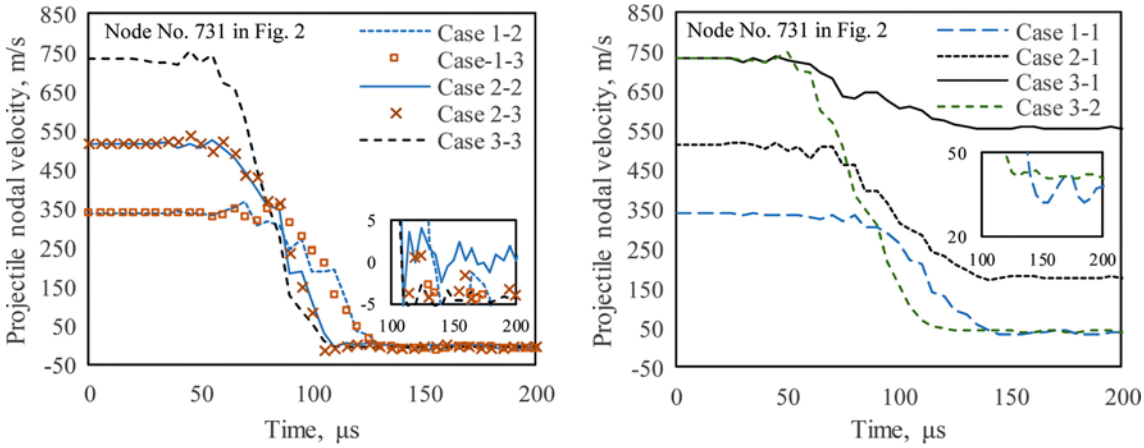

(a)

(b)

Fig. 5. Simulated Time Histories of the Projectile Velocity of a Typical Node (i.e., Node No. 731 shown in Fig. 2) for: (a) The Cases with Scabbing and Penetration Damage to the PC Slab, (b) The Cases with Perforation of the PC Slab

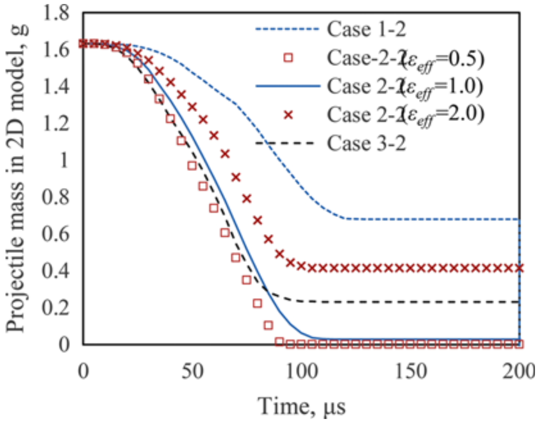

Fig. 6. Simulated Time History of the Mass of the Deformable Solid Projectile in Typical Cases

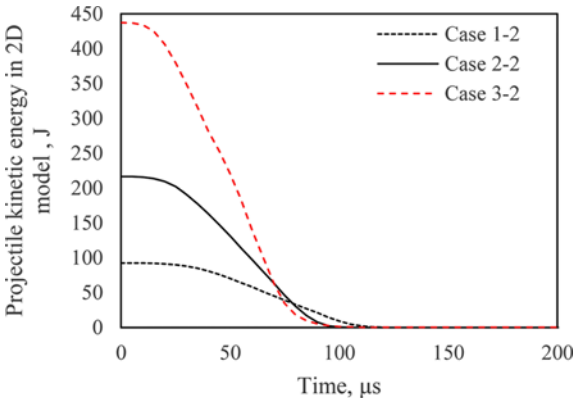

Fig. 7. Simulated Time History of the Kinetic Energy of the Deformable Solid Projectile in Typical Cases

in the case with a larger impact velocity, as shown in Fig. 5(a). This is because the erosion rate of the deformable solid projectile increases as the impact velocity increases, as shown by a decreasing tendency of the projectile mass with time in Fig. 6. Note that the mass of the projectile shown in Fig. 6 does not include the mass of deleted nodes due to the erosion. As a result, the energy dissipates much faster for the case with a larger impact velocity, as indicated in Fig. 7.

4.2 Simulated Perforation of the PC Slab

The simulated local damage of the PC slab for the other four cases, i.e., Case 1-1, Case 2-1, Case 3-1, and Case 3-2, is perforation and compares favorably well with the observation indicated in Figs. 3(e), 3(f) and Table 5. Fig. 8 shows the simulated perforation of the PC slab for these four cases after the impact in terms of the contour of the damage value D. It is found that some fragments of the deformable solid projectile pass through the PC slab in these four cases. In addition, both front and rear cratering are developed in Case 1-1, Case 2-1, and Case 3-1, as shown in Figs. 8(a), 8(b), and 8(c), respectively. Note that the only difference in these three cases is the impact velocity, as shown in Table 5. According to Chen *et al*. (2008), X and H^* shown in Fig. 8 are defined as the penetration depth and the residual thickness of rear crater for the normal perforation of a concrete target, respectively. The results show that as the impact velocity increases, the penetration depth X increases, while the residual thickness of rear crater H^* decreases. This tendency is similar to that found

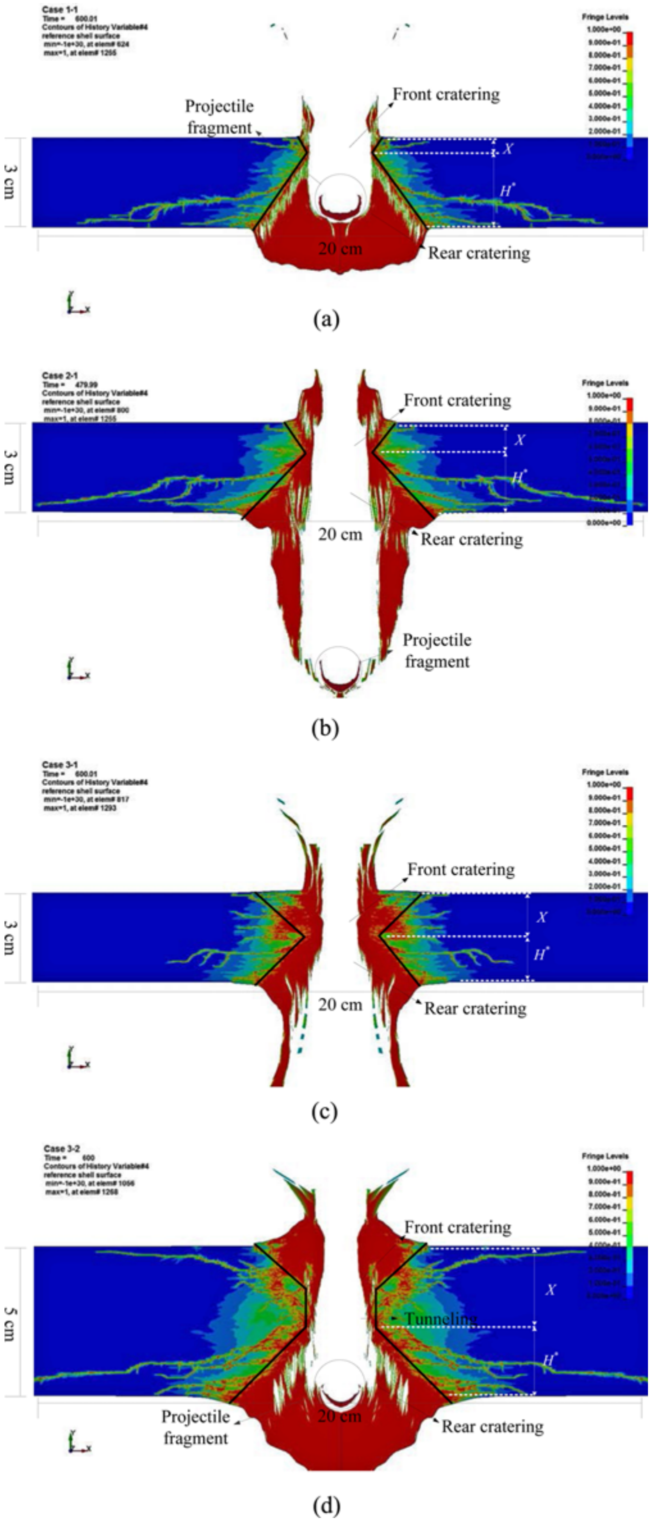

Fig. 8. Perforation of the Plain Concrete Slab for: (a) Case 1-1, (b) Case 2-1, (c) Case 3-1, (d) Case 3-2 (X: the penetration depth, H^*: the residual thickness of rear crater)

for a rigid projectile impact on a reinforced concrete target in a theoretical analysis that was reported by Chen *et al*. (2008). In addition, the residual velocity of the fragmented projectile increases as the impact velocity increases, as indicated in Fig. 5(b). Moreover, the comparison between Case 3-1 (see Fig. 8(b)) and 3–2 (see Fig. 8(d)) shows the effect of the slab thickness on the perforation of the PC slab. As the thickness of the PC slab increases, a tunneling in addition to the front and rear cratering is developed; this result numerically verifies the feasibility of the three-stage perforation model proposed by Chen *et al*. (2008) for the rigid projectile impact on thick concrete targets, although the solid projectile in this study is deformable.

5. Discussions

5.1 Mechanism of the Front Cratering and Scabbing of the PC Slab

To further illustrate the mechanism behind the front cratering and scabbing developed under the impact, Fig. 9 shows the simulated time histories of the pressure and the effective plastic strain at typical elements shown in Fig. 4(b) for Case 2-2. The results indicate that the peak pressure at the front cratering is compressive because of positive value, while it becomes tensile at the rear face. Thus, front cratering and scabbing are the result of compression failure and tensile failure of the PC slab, respectively. Moreover, after the failure of the PC slab, the effective plastic strain increases with time, as shown in Fig. 9(b) for the element Nos. 29884 and 1266. For the element No. 25277 representing the middle part of the PC slab, the damage value *D* is calculated to be approximately 0.42, indicating that no failure occurs. Thus, the effective plastic strain first increases and then remains unchanged with time. In addition, the tensile failure also occurs at the element No. 9207, which indicates the crack is developed inside the PC slab, especially along the bottom edge of the PC slab. Whether this crack occurred in the experiments is not reported by Tanaka and Ohno (2004). However, the occurrence of the crack is possible because the interior crack of the PC slab is not easy to accurately identify.

5.2 Mechanism of the Perforation of the PC Slab

Notably, shear plugging is typically responsible for the perforation of a concrete target under either soft impact (Koechlin and Potapov, 2009) or hard impact (Yankelevsky, 1997). However, in this study, the projectile penetration in addition to the shear plugging is found to cause the perforation of the PC slab under the impact of deformable solid projectiles. The perforation in Case 1-1 and Case 3-2 is the consequence of a shear cone breaking away, i.e., shear plugging, as shown in Figs. 8(a) and 8(d); while the perforation in other two cases, i.e., Case 2-1 and Case 3-1, is the result of projectile penetration, as shown in Figs. 8(b) and 8(c). Thus, the mechanism for the perforation caused by the impact of the deformable solid projectile depends on the impact velocity and the thickness of the PC slab.

5.3 Effect of Impact Velocity on the Maximum Penetration Depth

Additional cases are numerically studied by increasing the impact velocity of the deformable solid projectile to study the effect of the impact velocity on the maximum penetration depth. It is readily observed that the deformable solid projectile can easily perforate the slab with increasing impact velocity if the thickness of the concrete slab is small. Thus, a much thicker concrete slab is desirable for these cases. In this study, the thickness of the PC slab is assumed to be 14 cm so that the PC slab can be considered semi-infinite. The same finite mesh, material properties, contacts and boundary conditions used for the deformable solid projectile and PC slab are adopted in these cases.

Figure 10 shows the effect of impact velocity on the maximum penetration depth of the PC slab compared with the measurements, as well as a fitted curve derived in this study based on the numerical results. The maximum penetration depth of the slab increases exponentially with increasing impact velocity before a critical impact velocity is reached. This tendency is similar with that found from the results of the rigid projectile impact on a concrete target (Wang *et al*., 2007; Teland and Sjøl, 2004). However, beyond the critical velocity, the maximum penetration

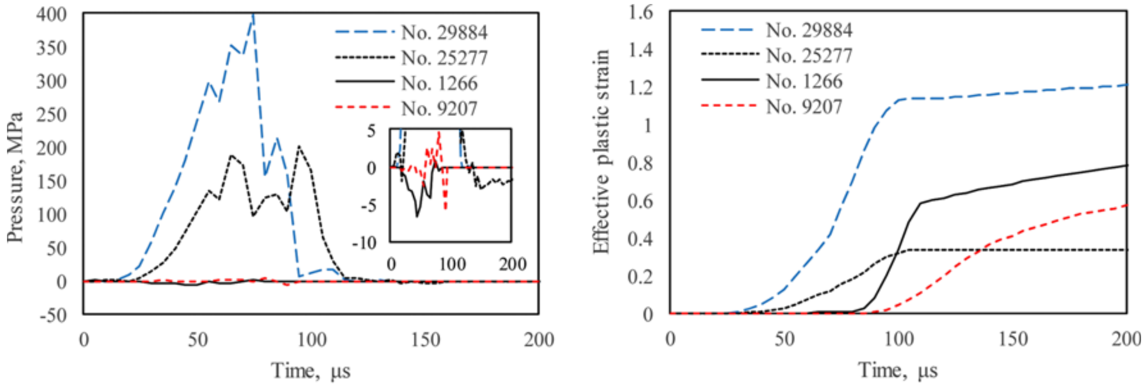

(a) (b)

Fig. 9. Simulated Time Histories of: (a) The Pressure,(b) The Effective Plastic Strain at Typical Elements in Case 2-2 (See the element No. in Fig. 4(b))

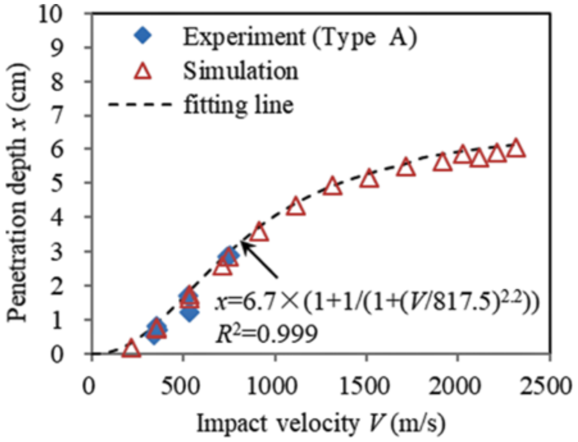

Fig. 10. Effect of the Impact Velocity on the Maximum Penetration Depth of the Plain Concrete Slab (compared with the measurements as well as a fitted curve derived in this study)

depth of the slab increases more slowly with increasing impact velocity and tends to reach a steady value. This steady value results form that the elements of deformable solid projectile can completely erode at high velocity. Thus, there is a limit value for the maximum penetration depth under the impact of deformable solid projectiles. A dose-response relation is employed to describe the variation of the maximum penetration depth of the PC slab with the impact velocity and is expressed in the following equation:

$$x = x_{\max}\left(1 - \frac{1}{1+\left(V/V_0\right)^n}\right) \tag{11}$$

where x is the maximum penetration depth of the PC slab (cm); V is the impact velocity of the deformable solid projectile (m/s); x_{max} is the limit value of the maximum penetration depth; V_0 is the critical impact velocity of the deformable solid projectile; and n is the fitting parameter. The fitting results show that the value of x_{max}, V_0, and n are approximately 6.7 cm, 817.5 m/s and 2.2, respectively. It is expected that the values of V_0, x_{max}, and n can be affected by various factors, such as, material properties of targets and deformable solid projectile and the size and the shape of the projectile. This needs further comprehensive investigations.

Moreover, attempts have been made to compare the numerical results with the available empirical relations available in published literature (Li and Tong, 2003), such as, Modified NDRC equation and BRL equation. The results show that existing empirical equations predict penetration depths several orders of magnitude greater than those observed in the simulation for the same impact velocity. This is probably because that existing empirical equations are proposed based on experimental data from rigid projectile impacts.

5.4 Local Damage of the PC Slab in the Hypothesis of the Rigid Projectile Impact

To investigate the effect of projectile rigidity on the local damage of the PC slab, two additional cases are numerically studied assuming that the projectile is rigid. The rigid projectile has the same mass and size as the deformable solid projectile and is modelled using the keyword *MAT_RIGID.

Figures 11(a) and 11(b) show the local damage of the PC slab in Case 2-3 and Case 2-1 in the hypothesis of the rigid projectile, respectively, in terms of the contour of the damage value D. The comparison between Fig. 4(a) with Fig. 11(a) shows that the maximum penetration depth under the impact of the rigid projectile is larger than that under the impact of the deformable solid projectile. In addition, the deformation of the PC slab in the case of the rigid projectile is much more localized (See Fig. 11(a)). This is because the nose of the rigid projectile is sharp and the contact area with the PC slab for the rigid projectile remains unchanged during the impact. The comparison between Fig. 8(b) and Fig. 11(b) shows that the damage area under the deformable solid projectile impact is much larger than that under the rigid projectile impact. This is because the contact area of the deformable solid projectile with the PC slab becomes larger during the impact due to projectile mushrooming, as shown by an increasing tendency of the diameter of the projectile over time in Fig. 12. As a result, the impact of the deformable solid projectile causes more damage to the PC slab when the PC slab is perforated. Thus, more attention should be paid to such an adverse effect of the deformable solid projectile impact on concrete targets.

5.5 Effect of the Erosion Strain Used for the Deformable Solid Projectile on the Local Damage of the PC Slab

The effect of the erosion strain used for the deformable solid

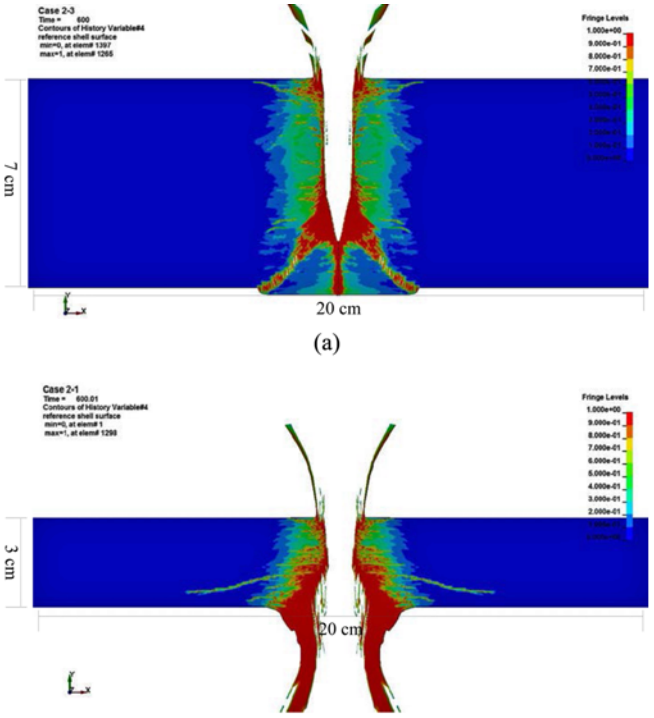

(a)

(b)

Fig. 11. Local Damage of the Plain Concrete Slab in: (a) Case 2-3, (b) Case 2-1 under the Rigid Projectile Impact

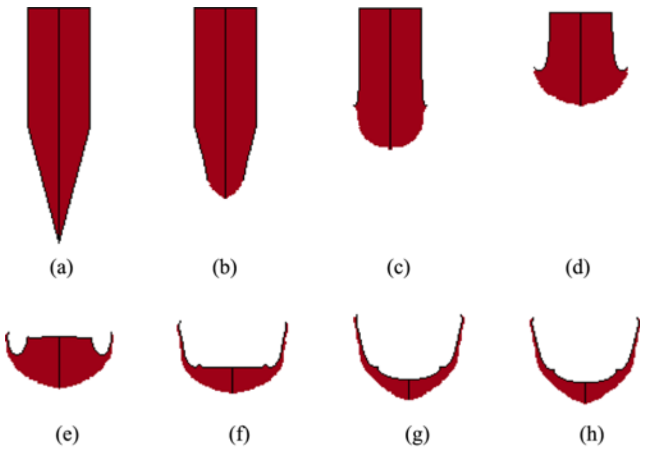

Fig. 12. Change of the Shape of the Deformable Solid Projectile in Case 2-1 Over Time: (a) 0 μs, (b) 20 μs, (c) 40 μs, (d) 60 μs, (e) 80 μs, (f) 100 μs, (g) 150 μs, (h) 200 μs

projectile on the local damage of the PC slab is presented by reducing the erosion strain used in a benchmark case. Case 2-2 shown in Fig. 4(b) is selected as the benchmark case. Figs. 13(a) and 13(b) show the local damage of the PC slab using 0.5 and 1.0 for the deformable solid projectile in the benchmark case, respectively. The results show that the damage area surrounding the bottom of the front cratering in the case using smaller erosion strain, as indicated by the dashed ellipse region in Fig. 13, is much larger than that in the benchmark case. This is because the erosion strain affects the mushrooming of the deformable solid projectile. If the erosion strain was small enough, the projectile mushrooming would disappear. Thus, when the erosion strain is decreased, the local damage is concentrated near the bottom of the front cratering of the PC slab, as shown in Fig. 13. The results also show that as the erosion strain decreases, the scabbing area near the rear surface decreases. This is because the elements of the deformable solid projectile with smaller erosion strain erode more quickly or completely erode during the impact, as shown in Fig. 6; thus, the rapid erosion or full erosion of projectile elements generates weaker compression stress waves that is shown in Fig. 14 and that could be well reflected from the rear surface and converted into tensile waves, causing scabbing.

5.6 Effect of the Damage Parameters of the RHT Model on the Local Damage of the PC Slab

To indicate the effect of the damage parameters of the RHT model on the local damage of the PC slab, Case 2-2 is reanalyzed by using the default damage parameters D_1 and D_2, i.e., $D_1 = 0.04$ and $D_2 = 1.0$, as reported by Borrvall and Riedel (2011). Fig. 15 shows the damage of the PC slab after the impact for Case 2-2 using the default damage parameters. The comparison between Fig. 4(b) and Fig. 15 shows that the damage area near the front cratering calculated by the default damage parameters is much larger than that calculated by the modified damage parameters (i.e., $D_1 = 0.24$ and $D_2 = 2.0$), as illustrated by the dashed ellipse region in Fig. 15. This implies that the selection of appropriate damage parameters is very helpful for providing reasonable prediction of local damage to the PC slab compared with the measurements. Thus, Eq. (10) is recommended to modify the default damage parameters of the RHT concrete model to accurately simulate an impact response of the PC slab with respect to the experimental results.

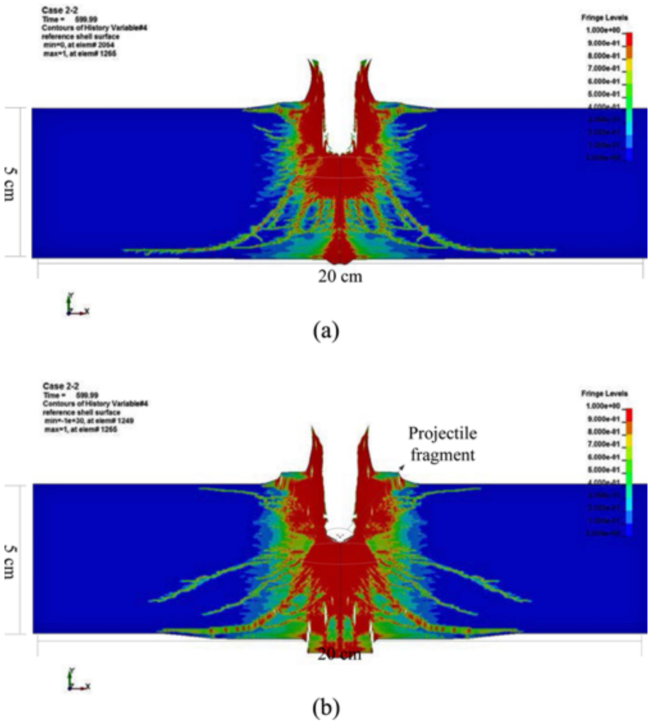

Fig. 13. Local Damage of the Plain Concrete Slab after Impact for Case 2-2 Using Different Erosion Strains: (a) 0.5, (b) 1.0

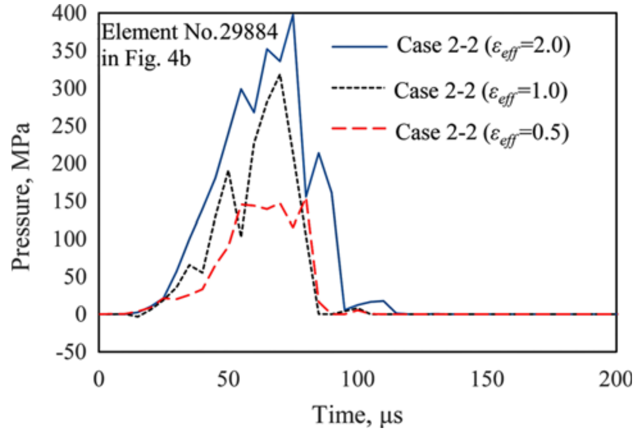

Fig. 14. Simulated Time Histories of the Pressure at the Element No. 29884 Shown in Fig. 4(b) for Case 2-2 with Different Erosion Values of the Maximum Equivalent Plastic Strain at Failure

6. Conclusions

In this study, an explicit dynamic finite element procedure, LS-DYNA, is employed to study nine existing experimental tests on

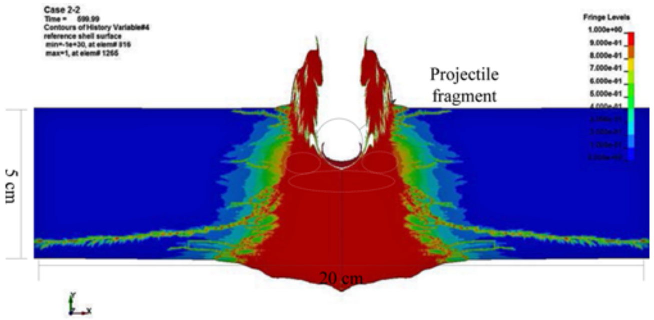

Fig. 15. Damage of the Plain Concrete Slab after Impact in Case 2-2 Using Default Damage Parameters, i.e., D_1 = 0.04 and D_2 = 1.0

the normal impact of a deformable solid (lead) projectile into a PC slab. The Steinberg model (#11) and the RHT model (#272) are used to characterize the dynamic response of the deformable solid projectile and the PC slab, respectively. Based on the numerical results, the following conclusions can be obtained:

1. The simulation results correspond well with the experimental results in terms of different modes of local damage to the PC slab and the maximum penetration depth of the PC slab;
2. Both projectile penetration and shear plugging are responsible for the perforation of the PC concrete under the impact of the deformable solid projectile.
3. In general, a typical two-stage perforation (i.e., front cratering, rear cratering) is obtained for a PC slab with a thickness of 3 cm under an impact velocity larger than 337 m/s, while a typical three-stage perforation (i.e., front cratering, tunneling, and rear cratering) occurs for a PC slab with a thickness of 5 cm under an impact velocity of 732 m/s. Moreover, as the impact velocity increases, the penetration depth increases, while the residual thickness of rear crater decreases.
4. As the impact velocity of the deformable solid projectile increases, the maximum penetration depth of the PC slab increases exponentially before a critical impact velocity is reached; however, beyond the critical velocity, the maximum penetration depth increases slowly and tends to reach a steady value. A dose-response relation can be used to describe the variation of the maximum penetration depth with the impact velocity for the deformable solid projectile;
5. The maximum penetration depth under the impact of the rigid projectile that has the same mass and size as the deformable solid projectile is larger than that under the impact of the deformable solid projectile; however, the deformable solid projectile can cause much more damage on the PC slab than the rigid projectile when the PC slab is perforated. This is because of the mushrooming of the deformable solid projectile during the impact;
6. The erosion strain used for the deformable solid projectile significantly affects the mushrooming of the projectile and thus affects the local damage of the PC slab.

Acknowledgements

This research was supported by the National Natural Science Foundation of China (Grant No. 51508271) and the Natural Science Foundation of Jiangsu Province of China (Grant No. BK20150958); these are gratefully acknowledged.

ORCID

Ling-Yu Xu https://orcid.org/0000-0001-6254-6242

References

Adams, B. (2003). *Simulation of ballistic impacts on armored civil vehicles*, MSc Thesis, Eindhoven University of Technology, Eindhoven, Netherlands.

Aquelet, N. and Souli, M. (2008). "2D to 3D ALE mapping." *Proc. of 10th Int. LS-DYNA Users Conference*, Detroit, MI, USA, pp. 23-34.

Borrvall, T. and Riedel, W. (2011), "The RHT concrete model in LS-DYNA." *Proc. of 8th European LS-DYNA Users Conference*, Strasbourg, France.

Chen, W. F. and Duan, L. (2003). *Bridge engineering: Seismic design*, CRC Press, Boca Raton, FL, USA.

Chen, X. W. and Li, Q. M. (2004). "Transition from nondeformable projectile penetration to semihydrodynamic penetration." *Journal of Engineering Mechanics*, Vol. 130, No. 1, pp. 123-127, DOI: 10.1061/(ASCE)0733-9399(2004)130:1(123).

Chen, X. W., Li, X. L., Huang, F. L., Wu, H. J., and Chen, Y. Z. (2008), "Normal perforation of reinforced concrete target by rigid projectile." *International Journal of Impact Engineering*, Vol. 35, No. 10, pp. 1119-1129, DOI: 10.1016/j.ijimpeng.2008.01.002.

Cox, P. A., Mathis, J., Wilt, T., Chowdhury, A., and Ghosh, A. (2006). "Assessment of structural robustness against aircraft impact at the potential repository at yucca mountain — Progress report II." *Center for Nuclear Waste Regulatory Analyses*, San Antonio, TX, USA.

Cui, J., Hao, H., and Shi, Y. (2018). "Study of concrete damage mechanism under hydrostatic pressure by numerical simulations." *Construction and Building Materials*, Vol. 160, pp. 440-449, DOI: 10.1016/j.conbuildmat.2017.11.083.

Ding, Y. Q., Tang, W. H., Zhang, R. Q., and Ran, X. W. (2013). "Determination and validation of parameters for Riedel-Hiermaier-Thoma concrete model." *Defense Science Journal*, Vol. 63, No. 5, pp. 524-530.

Eibl, J. (1987). "Soft and hard impact." *Proc. of the 1st Int. Con. on Concrete for Hazard Protection*, Edinburgh, Scotland, pp. 175-186.

Forrestal, M. J. and Piekutowski, A. J. (2000). "Penetration experiments with 6061-T6511 aluminum targets and spherical-nose steel projectiles at striking velocities between 0.5 and 3.0 km/s." *International Journal of Impact Engineering*, Vol. 24, No. 1, pp. 57-67, DOI: 10.1016/S0734-743X(99)00033-0.

Hazell, P. J., Fellows, N. A., and Hetherington, J. G. (1998). "A note on the behind armour effects from perforated alumina/aluminium targets." *International Journal of Impact Engineering*, Vol. 21, No. 7, pp. 589-595, DOI: 10.1016/S0734-743X(98)00014-1.

Hong, J., Fang, Q., Chen L., and Kong X. (2018). "Numerical predictions of concrete slabs under contact explosion by modified K&C material model." *Construction and Building Materials*, Vol. 155, pp. 1013-1024, DOI: 10.1016/j.conbuildmat.2017.08.060.

Kennedy, R. P. (1976). "A review of procedures for the analysis and design of concrete structures to resist missile impact effects." *Nuclear Engineering and Design*, Vol. 37, No. 2, pp. 183-203, DOI: 10.1016/0029-5493(76)90015-7.

Khoda-Rahmi, H., Fallahi, A., Liaghat, G. H. (2006). "Incremental deformation and penetration analysis of deformable projectile into semi-infinite target." *International Journal of Solids and Structures*, Vol. 43, No. 3, pp. 569-582, DOI: 10.1016/j.ijsolstr.2005.06.072.

Koechlin, P. and Potapov, S. (2009). "Classification of soft and hard impacts — Application to aircraft crash." *Nuclear Engineering and Design*, Vol. 239, No. 4, pp. 613-618, DOI: 10.1016/j.nucengdes.2008.10.016.

Kojima, I. (1991). "An experimental study on local behavior of reinforced concrete slabs to missile impact." *Nuclear Engineering and Design*, Vol. 130, No. 2, pp. 121-132, DOI: 10.1016/0029-5493(91)90121-W.

Lee, W. H. and Painter, J. W. (1999). "Material void-opening computation using particle method." *International Journal of Impact Engineering*, Vol. 22, No. 1, pp. 1-22, DOI: 10.1016/S0734-743X(98)00041-4.

Leppänen, J. (2006). "Concrete subjected to projectile and fragment impacts: Modelling of crack softening and strain rate dependency in tension." *International Journal of Impact Engineering*, Vol. 32, No. 11, pp. 1828-1841, DOI: 10.1016/j.ijimpeng.2005.06.005.

Li, Q. M. and Tong, D. J. (2003). "Perforation thickness and ballistic limit of concrete target subjected to rigid projectile impact." *Journal of Engineering Mechanics*, Vol. 129, No. 9, pp. 1083-1091, DOI: 10.1061/(ASCE)0733-9399(2003)129:9(1083).

LSTC (2014). *LS-DYNA keyword user's manual-Version R7.1*, Livermore Software Technology Corporation, Livermore, CA, USA.

Lou, J. F., Zhang, Y. G., Wang, Z., Hong, T., Zhang, X. L., and Zhang, S. D. (2014). "Long-rod penetration: The transition zone between rigid and hydrodynamic penetration modes." *Defence Technology*, Vol. 10, No. 2, pp. 239-244, DOI: 10.1016/j.dt.2014.05.007.

Luccioni, B. M., Aráoz, G. F., and Labanda, N. A. (2013). "Defining erosion limit for concrete." *International Journal of Protective Structures*, Vol. 4, No. 3, pp. 315-340, DOI: 10.1260/2041-4196.4.3.315.

Lv, T. H., Chen, X. W., and Chen, G. (2018). "The 3D meso-scale model and numerical tests of split Hopkinson pressure bar of concrete specimen." *Construction and Building Materials*, Vol. 160, pp. 744-764, DOI: 10.1016/j.conbuildmat.2017.11.094.

Mohotti, D., Ngo, T., and Mendis, P. (2013). "Numerical simulation of impact and penetration of ogvial shaped projectiles through steel plate structures." http://dl.lib.mrt.ac.lk/bitstream/handle/123/9547/SEC-11-183.pdf?sequence=1 [Accessed on July 5, 2016].

Ohno, T., Uchida, T., Matsumoto, N., and Takahashi, Y. (1992). "Local damage of reinforced concrete slabs by impact of deformable projectiles." *Nuclear Engineering and Design*, Vol. 138, No. 1, pp. 45-52, DOI: 10.1016/0029-5493(92)90277-3.

Pontiroli, C., Rouquand, A., Daudeville, L., and Baroth, J. (2012). "Soft projectile impacts analysis on thin reinforced concrete slabs: Tests, modelling and simulations." *European Journal of Environmental and Civil Engineering*, Vol. 16, No. 9, pp. 1058-1073, DOI: 10.1080/19648189.2012.699745.

Prakash, A., Srinivasan, S. M., and Rao, A. R. M. (2015). "Numerical investigation on steel fibre reinforced cementitious composite panels subjected to high velocity impact loading." *Materials & Design*, Vol. 83, pp. 164-175, DOI: 10.1016/j.matdes.2015.06.001.

Steinberg, D. J., Cochran, S. G., and Guinan, M. W. (1980). "A constitutive model for metals applicable at high-strain rate." *Journal of Applied Physics*, Vol. 51, No. 3, pp. 1498-1504, DOI: 10.1063/1.327799.

Tai, Y. S., Chu, T. L., Hu, H. T., and Wu, J. Y. (2011). "Dynamic response of a reinforced concrete slab subjected to air blast load." *Theoretical and Applied Fracture Mechanics*, Vol. 56, No. 3, pp. 140-147, DOI: 10.1016/j.tafmec.2011.11.002.

Tanaka, N. and Ohno, T. (2004). "Examine the local damage of concrete plate subjected to hypervelocity oblique impact of small projectile." *Proc. of 7th Symposium on the Impact Problem of the Structure*, Japan Society of Civil Engineering, Vol. 7, pp. 147-152 (in Japanese).

Teland, J. A. and Sjøl, H. (2004). "Penetration into concrete by truncated projectiles." *International Journal of Impact Engineering*, Vol. 30, No. 4, pp. 447-464, DOI: 10.1016/S0734-743X(03)00073-3.

Wang, Z. L., Li, Y. C., Shen, R. F., and Wang, J. G. (2007). "Numerical study on craters and penetration of concrete slab by ogive-nose steel projectile." *Computers and Geotechnics*, Vol. 34, No. 1, pp. 1-9, DOI: 10.1016/j.compgeo.2006.09.001.

Wen, H. M. and Xian, Y. X. (2015). "A unified approach for concrete impact." *International Journal of Impact Engineering*, Vol. 77, pp. 84-96, DOI: 10.1016/j.ijimpeng.2014.11.015.

Wilt, T., Chowdhury, A., and Cox, P. A. (2011). "Response of reinforced concrete structures to aircraft crash impact." *US Nuclear Regulatory Commission Contract NRC-02-07-006*, San Antonio, TX, USA.

Xu, L. Y., Cai, F., Wang, G. X., Chen, G. X., and Li, Y. Y. (2017). "Nonlinear analysis of single reinforced concrete piles subjected to lateral loading." *KSCE Journal of Civil Engineering*, KSCE, Vol. 21, No. 7, pp. 2622-2633, DOI: 10.1007/s12205-017-1010-2.

Yankelevsky, D. Z. (1997). "Local response of concrete slabs to low velocity missile impact." *International Journal of Impact Engineering*, Vol. 19, No. 4, pp. 331-343, DOI: 10.1016/S0734-743X(96)00041-3.

Yi, S. T., Moon, Y. H., and Kim, J. K. (2005). "Long-term strength prediction of concrete with curing temperature." *Cement and Concrete Research*, Vol. 35, No. 10, pp. 1961-1969.